2D Materials 6.3 (2019): 035015

DOI: https://doi.org/10.1088/2053-1583/ab175c

A fast synthesis route of Boron-Carbon-Nitrogen ultrathin layers towards highly mixed ternary B-C-N phases

Fabrice Leardini[1,2]*, Nuria Jiménez-Arévalo[1], Isabel J. Ferrer[1,2], José Ramón Ares[1], Pablo Molina[1,2], Cristina Gómez Navarro[2,3], Yolanda Manzanares[3], Daniel Granados[4], Fernando J. Urbanos[4], F. Javier García-García[5], Adolfo del Campo[6], Giulia Avvisati[7], Maria Grazia Betti[7], Carlo Mariani[7]

[1] *Departamento de Física de Materiales, Universidad Autónoma de Madrid, Campus de Cantoblanco E-28049, Madrid, Spain*

[2] *Instituto Nicolas Cabrera, Universidad Autónoma de Madrid, Campus de Cantoblanco E-28049, Madrid, Spain*

[3] *Departamento de Física de la Materia Condensada, Universidad Autónoma de Madrid, Campus de Cantoblanco E-28049, Madrid, Spain*

[4] *Instituto Madrileño de Estudios Avanzados en Nanociencia (IMDEA-Nanociencia), Cantoblanco, E-28049, Madrid, Spain*

[5] *ICTS-Centro Nacional de Microscopía Electrónica, Universidad Complutense de Madrid, E-28040, Madrid, Spain*

[6] *ICV-CSIC (Instituto de Cerámica y Vidrio, Consejo Superior de Investigaciones Científicas), Campus de Cantoblanco, E-28049, Madrid, Spain*

[7] *Dipartimento di Fisica, Università di Roma 'La Sapienza', I-00185 Roma, Italy*

* Corresponding author: **fabrice.leardini@uam.es**

Keywords: Microwave-Assisted Plasma-Enhanced Chemical Vapor Deposition, Borocarbonitride, Optical Bandgap, Electronic Transport measurements, x-ray Photoelectron Spectroscopy, Raman spectroscopy, Transmission Electron Microscopy

Abstract

We report a direct and fast synthesis route to grow Boron-Carbon-Nitrogen layers based on microwave-assisted plasma enhanced chemical vapour deposition by using methylamine borane as a single source molecular precursor. This easy and inexpensive method allows controlled and reproducible growth of B-C-N layers onto thin Cu foils. Their morphological, structural, chemical, optical and transport properties have been thoroughly characterized by a number of different microscopies, transport and spectroscopic techniques. Though disorder and segregation into C-rich and h-BN-rich domains has been observed in ultrathin flat few layers, high doping levels have been reached, inducing strong modifications of the electronic, optical and transport properties of C-rich and h-BN-rich phases. This synthesis procedure can open new routes towards the achievement of homogeneous highly mixed ternary B-C-N phases.

1. Introduction

The search of semiconducting B-C-N ultra-thin layers has attracted enormous interest in recent times. As compared to Graphene (Gr) and h-BN, which behave as a semimetal and as an insulator, respectively, ternary B-C-N phases have been predicted to present an adjustable bandgap depending on the C/BN ratio [1,2]. Their growth thus represents a landmark, which can have important applications in nanoelectronics, optoelectronics and catalysis. However, the achievement of homogeneous graphitic-like B-C-N ternary phases with mixing of B-C, B-N, C-N and C-C bonds is hindered by the tendency of this ternary system towards segregation into distinct C-rich and h-BN-rich phases [1,3]. This is related to the fact that C-C and B-N bonds are thermodynamically more stable than C-N and B-C ones. However, the existence of metastable homogeneous B-C-N ternary phases has been predicted by theoretical calculations [2]. One of the keys towards the achievement of these ternary phases seems to be related to the kinetic control of the growth process. Conventional chemical vapour deposition (CVD) methods have been extensively used to grow these ternary layers. In the seminal works, the use of different precursors containing C and B-N atoms (typically CH_4 or C_2H_6 and NH_3BH_3) was investigated [4-6]. More recently, the use of single-source precursors containing B, C and N atoms has been also explored, aimed by the expectation of a higher mixing (in terms of bonding types) in the obtained B-C-N layers. Among these

molecular precursors we can find trimethylamine borane [7], dimethylamine borane [8] and methylamine borane (MeAB hereafter) [9]. The growth of these ternary B-C-N layers has been usually done onto Cu foil substrates, due to the low solubility of these atoms on Cu as well as to the easy transferability of the obtained layers onto other substrates, which is necessary for their complete characterization. In spite of all these efforts, the achievement of these homogeneous B-C-N phases remains elusive. Most of the previous works have shown that ternary B-C-N layers are composed of a patchwork of C-rich and h-BN domains [4-9]. The presence of some C-N bonds has been also observed, but these are in a relatively low amount and seem to come mainly from C-N interactions at the edges of the different phase domains. A recent work reports the growth of Gr-like B-C-N monolayers by using bis-BN cyclohexane [10] as a single source precursor on the Ir(111) surface. Based on scanning tunnelling microscopy, x-ray photoelectron spectroscopy and according to Density Functional Theory calculations, authors state the achievement of a homogeneous ternary B-C-N phase. However, as far as we know, experimental confirmations of a bandgap opening in this system based on transport or spectroscopic measurements are still lacking. Moreover, the growth method uses a precious single-crystalline substrate and a molecular precursor whose synthesis is quite complex [11].

This work explores an ultrafast and viable growth method aiming at the achievement of metastable highly mixed ternary B-C-N phases with planar bonds among the three elements. The method reported here is quite easy and uses a cheap Cu foil substrate and a relatively simple molecular precursor. It consists of microwave-assisted plasma enhanced chemical vapour deposition (PECVD) by using MeAB as a single source precursor. The microwave-assisted PECVD growth is done in a sealed glass ampoule containing the metallic substrate and the MeAB precursor, which is irradiated by using a conventional microwave oven. This is a very fast synthesis method (few seconds) and uses tiny amounts of the molecular precursor and low electricity consumption. This contrasts with conventional CVD methods, which are more time consuming and use large amounts of processing gases (such as Ar and H_2) and electrical energy consumption, making them much more expensive in terms of manufacturing costs.

The obtained B-C-N layers have been thoroughly characterized, in order to clearly elucidate their morphology, structure, chemical composition and bonding types, and how these affect the electronic, optical and transport properties. The fast growth

mechanism produces highly disordered layers, with presence of C-rich and h-BN-rich domains with different orientations. However, our results clearly demonstrate that much more homogeneous mixing of B, C and N atoms is reached, as compared to conventional CVD methods. Actually, high doping levels of N and B in C-rich domains and of C in h-BN-rich regions are obtained. This fact produces important modifications of the optical absorption bands and electronic transport properties of the C-rich and h-BN-rich phases. As previously stated, none of the numerous previous works on this system has demonstrated the successful growth of ternary B-C-N homogeneous layers with semiconducting properties. This is due to the strong tendency towards segregation in C-rich and h-BN-rich nanodomains. Accordingly, the reported optical properties of B-C-N layers are quite similar, regardless their global B:C:N contents. The optical absorption spectra of these layers always present two peaks, one with an absorption maximum at 268-270 nm due to C-rich regions and another feature peaking around 210 nm due to h-BN regions [4,5,9]. The changes in the global B:C:N composition in the layers only affect to relative peak intensities (the C-rich optical absorption peak increases when increasing the relative C content). However, previous literature data show almost the same peak positions for these absorption peaks, which may be related to small doping levels of C-rich regions by B and N (and vice versa). Here we demonstrate clear modifications in the peak positions of the optical absorption spectra induced by a change in the kinetic growth mechanism which leads to a much more mixed scheme in terms of bonding types. This in turn modifies the electronic transport properties of B-C-N layers (showing intrinsic n-type conductivity) as compared to previous works (showing an ambipolar character). Although the use of a single source molecular precursor (such as MeAB) does not allow changing the relative B:C:N contents in the obtained layers, different global compositions may be obtained by changing the chemical composition of the molecular precursor used in microwave-assisted PECVD process. The present work thus paves the way for the achievement of homogeneous bonding and mixing of B, C and N and open new routes towards the growth of semiconducting ternary B-C-N phases.

2. Experimental details

2.1 Synthesis of B-C-N layers

Borocarbonitride layers have been grown by microwave-assisted PECVD. Several substrates have been investigated for microwave-assisted PECVD growth, such as Cu foil (Alfa Aesar, 99.8%, 25 μm thickness), Silicon (Si wafers doped with Boron, p-type, thickness of 500-550 μm, <100> orientation) and quartz slides (SPI supplies, 1 mm of thickness). The substrates were cleaned in an ultrasound bath first in acetone and then in ethanol and placed into Pyrex ampoules, which can be hermetically closed with a valve and introduced in a glove box (MBraun, < 1 ppm H_2O, <10 ppm O_2). The precursor containing B, C and N atoms used for microwave-assisted PECVD growth was MeAB, which was synthesized and characterized following the procedure reported elsewhere [9], and subsequently stored and handled in a glove box. About 1 mg of MeAB powder was placed at the bottom of the Pyrex ampoules by using a large funnel. Then, the ampoules containing the substrate and the precursor under Ar atmosphere were taken out of the glove box and connected to a diffusion pump, in order to fuse and seal them under a residual vacuum in the 10^{-6} mbar range. The bottom part of the ampoules, where MeAB was placed, was immersed in a liquid nitrogen bath in order to avoid MeAB sublimation during the sealing of the ampoules in vacuum. Once the sealed ampoules acquire the room temperature, the MeAB partially sublimates until reaching a pressure around $6 \cdot 10^{-3}$ mbar (its vapour pressure) [12]. Next, the ampoules were placed at the centre of a conventional microwave oven (2.45 GHz, 800 W) and irradiated for a few seconds. A plasma was then created inside the ampoules. The optical emission spectrum of the plasma has been collected with an optical fibre and recorded with a CCD spectrometer (Ocean, mod. Flame) in the 190-860 nm range.

2.2 Experimental methods

The as-grown samples on the different substrates have been characterized by Raman spectroscopy in a WITec ALPHA 300AR instrument using a confocal microscope with different lenses (20x and 100x). A laser with excitation wavelength of 532.25 nm and a power of 2 mW has been used. Further Raman characterizations of layers transferred onto different substrates have been done at 488 nm and 785 nm excitation wavelengths. Spectra acquired at 488 nm were carried out with a diffraction grating spectrometer (0.5

m) and an electron multiplied Peltier Cooled Si-CCD. Spectra were acquired in a confocal set up with a X40 plan-apo microscope objective with a N.A. of 0.65. Excitation power was kept below 2.5 mW. Raman spectra with the 785 nm diode laser were carried out in a spectrometer InVia, Renishaw plc, UK using an excitation power <5 mW. The sharp silicon line located at 520 cm^{-1} was used as a reference in the Raman shift scale. The samples were placed into focus with an optical microscope employing a 50x magnification objective (Leica, Germany).

The morphology of the obtained layers has been analyzed by Optical Microscopy (OM) in an Olympus BX51 microscope with a Nomarsky filter, Scanning Electron Microscopy (SEM) in a Hitachi S3000 instrument and by Field Emission Gun (FEG) measurements in a Philips XL30 S-FEG apparatus.

In order to further characterize the layers grown on Cu foils, these have been transferred onto different substrates, such as Si wafers described before, Si/SiO_2 (IDB Technologies, Si wafers with orientation <100>, and thickness of 525 μm, capped with 285 nm of SiO_2) and SiO_2 (SPI supplies, 1 mm of thickness). The transfers have been done in a clean room, by capping with PMMA and chemically etching the Cu, following the procedure reported in [9].

The obtained layers have been further characterized by means of a plethora of techniques, in order to determine their structure, morphology, chemical composition, optical and electronic transport properties.

Atomic Force Microscopy measurements

Atomic Force Microscopy (AFM) images were acquired in non-contact mode with a homemade microscope controlled with a Dulcinea Control Unit (Nanotec) and WSxM software [13]. Silicon AFM probes from Nanosensors with a nominal force constant of 40 N/m, resonant frequency of ~ 350 kHz and tip radius of 20 nm were used for the measurements. B-C-N layers imaged by AFM were transferred onto Si/SiO_2 substrates.

Transmission Electron Microscopy characterization

The obtained B-C-N layers were also characterized by High-Resolution Transmission Electron Microscopy (HRTEM), Selected Area Electron Diffraction (SAED) and Electron Energy Loss Spectroscopy (EELS). Prior to the high-resolution work we

analyzed the specimens in a JEOL 2100HT, operated at 200 kV. At this stage, we performed the SAED experiments. A JEOL JEM 3000F transmission electron microscope operated at 300 kV was used for the high-resolution imaging. This scope is attached with an ENFINIUM SE spectrometer, which was used for the recording of the Spectrum Imaging and EELS data.

Transfer of the B-C-N layers onto the TEM grids was done by scrapping the layers (grown on the Cu foils) with a scalpel onto the Cu grids. Optical microscopy coupled with Raman spectroscopy was employed in order to check the transfer process before performing TEM measurements (See the Supplementary Material).

X-ray Photoelectron Spectroscopy measurements

The X-ray Photoelectron Spectroscopy (XPS) measurements were carried out at the LoTUS surface physics laboratory (Sapienza, University of Rome, Italy) in an Ultra High Vacuum (UHV) chamber, with a base pressure in the low 10^{-10} mbar range. Photoelectrons were excited by an AlK_{α} photon source ($h\nu$ = 1486.7 eV) and they were measured with a hemispherical electron analyser (VG Microtech Clam-2) used in constant pass energy (PE) mode set at 50 eV, with an energy resolution of 1 eV, further details are available in [9, 14,15]. The electron binding energy (BE) was calibrated by acquiring after each measurement the Au $4f_{7/2}$ core-level set at 84.0 eV BE. The microwave-assisted PECVD- sample grown on Cu was air-transferred and mounted in the XPS ultra-high-vacuum system. The sample was annealed up to 480 °C in UHV in sequential steps, and after each step XPS spectra were acquired at RT, until the C 1s lineshape reached a saturation value (see temperature evolution in the Supplementary Material).

Optical Absorption Spectroscopy

The absorption spectra were recorded with a double beam UV/vis/NIR Lambda 1050 PerkinElmer spectrometer. The samples were measured in transmission configuration using a spot size of 5 mm^2 in the 190-800 nm spectral range. The B-C-N layers were transferred onto quartz substrates. Baselines for the instrument calibration were recorded before the measurements. These baselines were measured by using two quartz slides, one in the reference channel and another one in the sample channel. Then, the layers transferred onto the quartz slides were measured by putting them in the sample channel, while maintaining a quartz slide in the reference channel. In this way, the

optical density of the layers is obtained in a direct way. Afterwards, bare quartz slides were measured by putting these in the sample channel, while maintaining another quartz slide in the reference channel, giving flat signals and thus confirming the validity of the recorded baselines.

Electrical conductance/transport measurements

For the electrical conductivity measurements, we prepared bottom-gated field-effect transistors (FETs) by transferring the B-C-N layers onto highly doped silicon substrates with 285 nm of oxide layer (Si/SiO_2 substrates). Gold contacts (to act as electrodes) were deposited on top of the layers by thermal evaporation using a stencil mask. The layers, bridging the source and drain electrodes, behaved as the conducting channel. The channel length and width were 2 μm and 19 μm, respectively. Measurements have been recorded under a vacuum in the 10^{-5} mbar range. FETs devices were held in vacuum for at least two days before the measurements, in order to suppress the possible influence of adsorbed species on the recorded drain current.

3. Results and discussion

3.1 Morphological and structural properties of the B-C-N layers

The emission spectrum of the plasma created inside the ampoules during the growth process (see the Supplementary Material, Figure S1) presents the most intense emission lines characteristic of H, CN, NH and C_2 groups [16], indicating that the plasma is composed by radicals containing the atoms present in the molecular precursor. It is worth to mention that temperature inside the ampoules can reach extremely high values, eventually leading to the fusion of the Cu substrates when these are exposed to the plasma induced by microwave radiation during 10 seconds or higher exposure times. Therefore, the plasma was maintained typically during 5 seconds for microwave-assisted PECVD growth. The layers grown on the Cu substrates present a homogeneous flat morphology, as observed by OM and SEM images of the as-grown samples (see the Supplementary Material, Figures S2a and S4b) as well as of samples transferred onto other substrates (see Figures S4a,c,d). Interestingly, these present a very small amount of impurities like nanoparticles and nanowires, which are usually observed in

conventional CVD growth of h-BN and B-C-N layers by using ammonia borane as a precursor [17-19].

The morphology of the obtained samples has been characterized by AFM measurements, after transfer onto flat Si/SiO_2 substrates. A representative AFM image of the B-C-N layers is shown in Figure 1a. The image shows a homogeneous film with some characteristic folding and wrinkles created during the transfer process. Several different regions in various samples have been imaged, showing high reproducibility (see the Supplementary Material, Figure S3), with an average sample thickness of 3±1 nm in the obtained layers on the whole surface (Figure 1b), when using a growth time of 5 s in the microwave-assisted PECVD process. An increase in layer thickness when increasing the growth time can be inferred (see Figure S3). Therefore, the present growth method allows a good control on the obtained layer thickness.

Raman spectroscopy is a very useful technique to characterize the homogeneity and the quality of the obtained B-C-N layers. The typical Raman spectra of the B-C-N layers deposited onto Si and of the bare Si substrate acquired with a 532 nm laser are shown in Figure 1c. Several Raman bands are observed with peak maxima around 1350 cm^{-1} (D band), 1600 cm^{-1} (G band), 2680 cm^{-1} (2D band) and 2920 cm^{-1} (D+G band). An additional shoulder appearing at 1625 cm^{-1} is also present, which is usually observed in high disordered and N-doped Gr [20,21] and B-C-N layers [4,5,9,22] and it is ascribed to the so-called D' band. In addition, a small peak is seen at 1450 cm^{-1}, due to the Si substrate. The Raman spectrum of the present samples is quite similar to those reported before in Gr [20,21] and in Gr/h-BN patchworks [4,5,9,22], and is indicative of sp^2 hybridization in the obtained B-C-N layers.

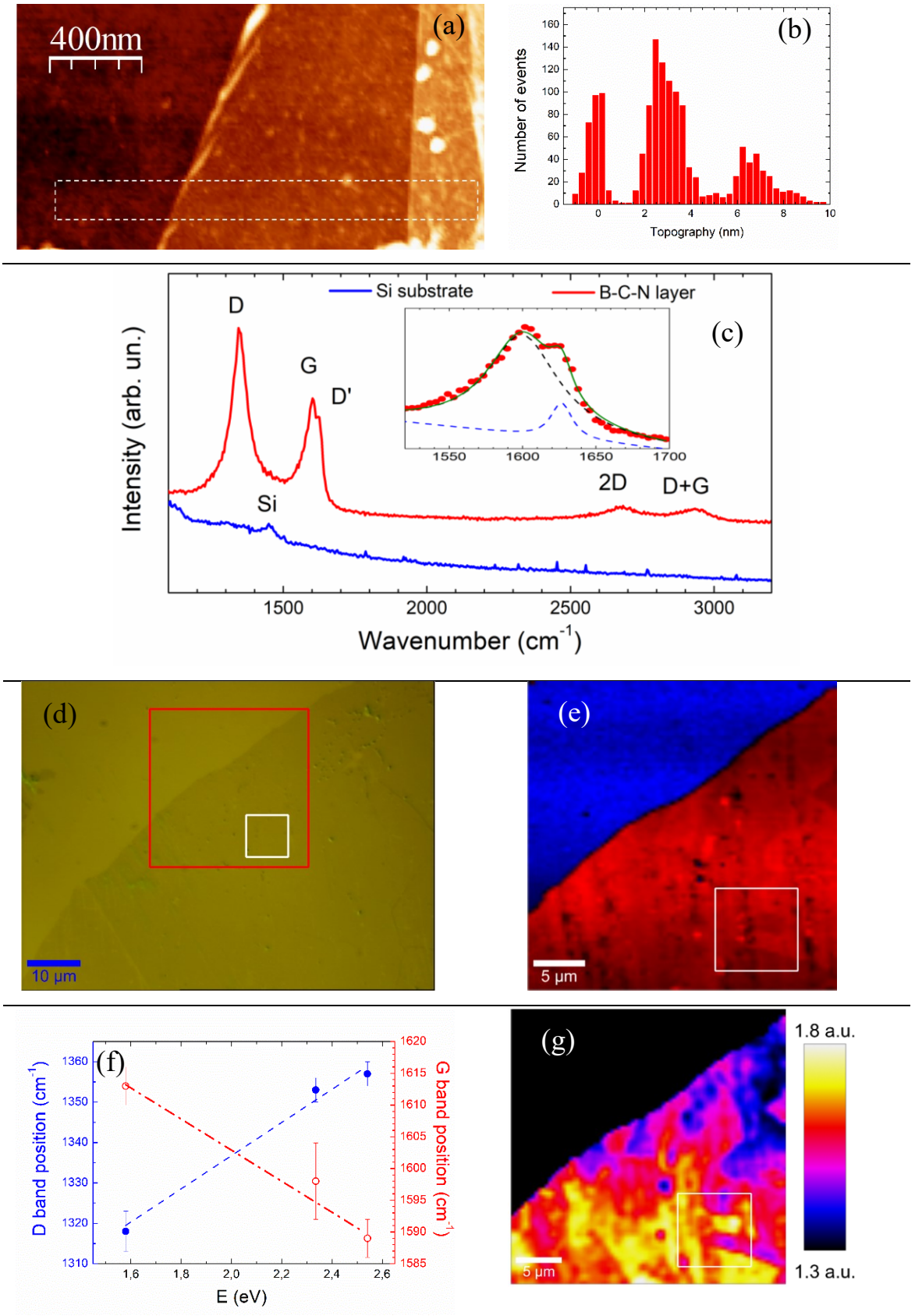

Figure 1. (a) AFM image of a B-C-N layer (orange and yellow regions) transferred onto a Si/SiO_2 substrate (darkest region at the left of the image); the layer is folded on the right part of the image (yellow zone), which is typically observed in transferred ultrathin layers, forming a

straight terrace. (b) Topography distribution histogram obtained from the region marked by the dashed line in the AFM image; the obtained thickness of the layer is of about 3 nm (notice the three different terraces with 3 nm-height, within the dashed line marked area). (c) Raman spectra (recorded at 532 nm excitation wavelength) of a B-C-N layer grown on Cu and transferred onto a Si substrate, and of the bare Si substrate as a reference. The inset shows the deconvolution of G and D' bands using Lorentzian peaks. (d) Optical image of a B-C-N layer transferred onto Si/SiO_2 substrate, showing the area used for Raman spectral mapping (red line). (e) Raman spectral mapping of the B-C-N layer; blue regions indicate the Si/SiO_2 substrate, whereas red ones the B-C-N layer. (f) Dispersion curves of the D and G band positions obtained at different excitation wavelengths; uncertainty bars have been determined by statistical analyses of the Raman spectra acquired in different regions. (g) Map of the D/G intensity ratio through the sample.

The homogeneity of the structural and bonding properties through the samples at micrometric scales has been characterized by Raman spectral mapping. Raman maps have been acquired at the edge of the transferred B-C-N layers, in zones showing the layers and the bare Si substrate. Regions of 30x30 μm^2 have been analysed, by recording 3600 spectra in each region (see Figures 1d and 1e). Each individual Raman spectrum of the maps contains the Raman bands of the B-C-N layers as well as those of the Si substrate. Therefore, each spectrum of the map (S) can be expressed as a linear combination of two basis spectra: the average spectrum of the Si substrate (B_1) and the average spectrum of the B-C-N layers (B_2): $S=a_1B_1+a_2B_2$. These two basis spectra have been obtained by averaging the recorded data sets in different zones of the sample. Then it is possible to estimate the weighting factors a_1 and a_2 by least squares fitting. The weighting factor is proportional to the scattering intensity of the material within the laser focus. Background is subtracted to all the spectra (linear background) prior to fitting procedures. In this way, a map showing the relative contributions of each basis spectra to the measured spectrum (i.e., the a_1 and a_2 values) is obtained, as shown in Figure 1e. Blue zones represent the Si substrate (a_1 values close to 1) whereas red ones indicate the B-C-N layer (zones with a_2 close to 1). In addition, the intensity ratio of the D and G Raman bands, which is indicative of the density of defects [23], has been mapped through the samples, as it can be seen in Figure 1g. These maps show some fluctuations both in the total and in the D/G relative intensities. The distribution of the peak positions of D and G Raman bands have been also analysed (see the Supplementary Material, Figure S6). These analyses enable the comparison of different

B-C-N samples, in order to characterize the reproducibility of their structural properties. The obtained results show broad distributions in the total intensity, the D and G peak positions, as well as in the intensity ratios. Therefore, both the layer thickness, the bonding properties and the defect concentrations present some inhomogeneities through the samples, induced by the disordered character of the layers. Anyway, the comparison of different samples gives a reasonably good reproducibility (see the Supplementary Material, Figure S6).

The dispersion of D and G peak positions and intensity ratios as a function of the laser excitation wavelength have been also investigated. Figure 1f plots the dispersion curves of D and G peak positions. The D band presents a positive dispersion with a slope of 41±6 cm^{-1} eV^{-1}, in agreement with the values reported in Gr, graphitic Carbon [24-26] and B-C-N layers [9]. On the other hand, the G band shows a negative dispersion, with a slope of -24±3 cm^{-1} eV^{-1}. This negative dispersion behaviour has been also reported in multi-layered Gr and graphite samples [25,26], as well as in B-C-N nanolayers [9] and has been ascribed to the presence of defects and stacking faults between the layers [27]. The higher slope of the present samples as compared to previous results suggests a higher disordered character of the samples. As it concerns the dispersion curves of the D/G intensity ratios (see the Supplementary Material, Figure S7), these do not show the reported linear dependence on the excitation wavelength to the fourth power, observed in Gr [23], graphitic Carbon [28] and B-C-N nanolayers [9]. This deviation suggests that the average distances between defects are below 3 nm [23], which implies a high density of defects in the present samples.

On the other hand, the deconvolution of G and D' peaks using Lorentzian functions (see the inset of Figure 1c) allows calculating the ratio between the intensities of D and D' Raman bands. This ratio provides useful information on the nature of the defects responsible of these peaks [74]. An average value of 4.1(5) has been obtained in the present samples, which is close to that observed for boundary-type defects [74]. This result excludes the presence of sp^3-type defects and points out a small size of crystalline domains in the layers.

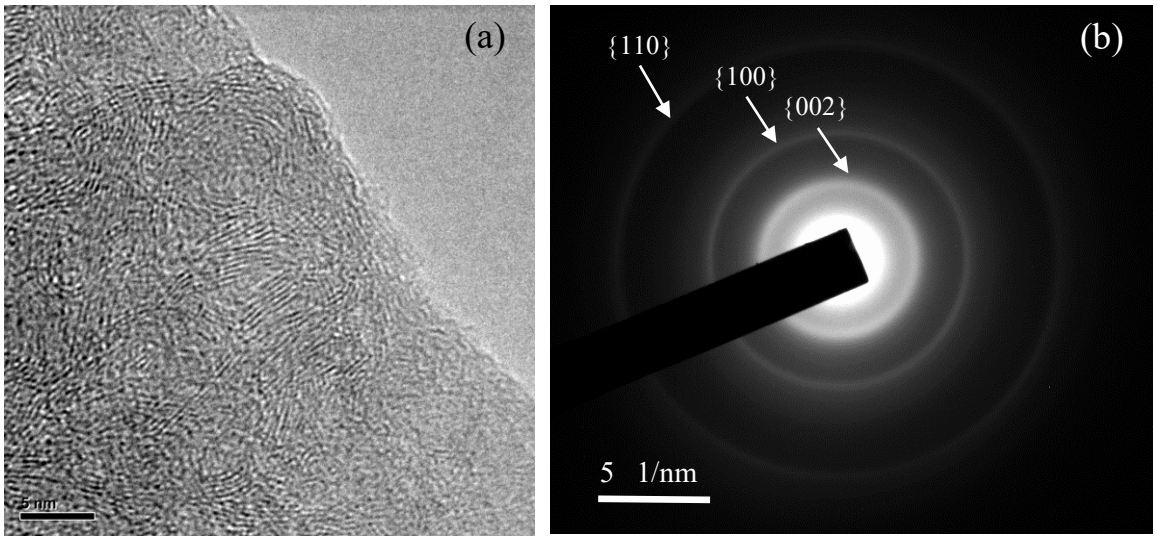

Figure 2. (a) TEM micrograph of B-C-N layer recorded at high magnification; (b) SAED pattern of the layer, which presents diffraction rings corresponding to a graphitic-like structure (diffracting planes corresponding to each ring are shown).

The morphology and structural properties of the B-C-N layers have been further characterized by TEM analysis. Figure 2a shows a representative high-resolution TEM micrograph. It can be clearly seen that B-C-N layers are composed of very small nanodomains and that there exists no order between them. These are disposed along different orientations giving rise to a disordered atomic structure. The consequence is that the SAED patterns (Figure 2b) present three diffraction rings distinguishable from the background, which correspond to interplanar distances of 1.3±0.1 Å, 2.2±0.1 Å and 3.5±0.2 Å. These diffraction rings can be indexed to first order reflections of {110}, {100} and {002} planes in the hexagonal graphitic-like structure [29], respectively. It is quite remarkable the growth of the B-C-N nanodomains with {002} planes normal to the plane of the B-C-N layers. This observation has been previously reported in B-C-N layers obtained by PECVD [30], but it is not observed when using conventional CVD growth [4,9]. On the other hand, the observation of continuous diffraction rings in SAED patterns indicates the polycrystalline nature of the B–C–N layers, which are composed by very small crystalline domains having typical sizes below a few nanometers. A graphitic-like structure composed of nanocrystalline domains and with strong disorder is thus evident in the obtained layers, in good accordance with Raman data.

In order to avoid the transfer process of B-C-N layers onto other substrates, which is necessary for their characterization by different techniques, we have also investigated the direct growth of B-C-N layers by microwave-assisted PECVD on SiO_2 and Si substrates. The obtained results show that quartz substrates do not act as catalysts for the splitting of MeAB molecules and, therefore, no deposition of B-C-N layers occurs. On the contrary, a deposit consisting in small droplets of the MeAB precursor (perhaps slightly polymerized) is observed on the surface of the quartz substrate (see the details in the Supplementary Material, Figure S8). This suggests that MeAB precursor sublimates during the microwave irradiation process and afterwards, gaseous MeAB molecules present in the ampoule first condensate and then solidify on the substrate during their cooling after exposure to microwave radiation, without reacting on the quartz surface to form B-C-N layers.

Silicon substrates are also quite inert for microwave-assisted PECVD growth of B-C-N layers and only a few dispersed nanoparticles were observed on the clean Si surface. Raman spectra of these nanoparticles suggest that these present a graphitic-like structure and may be composed of B, C and N (see the Supplementary Material, Figure S9). However, no evidence of the growth of a homogeneous layer on the Si substrate was obtained. This suggests that nucleation and growth take place only at special points (presumably related to defects) at the Si surface. All these results point out the important role of the surface of the substrate for the catalytic CVD process, even when it is activated by a plasma, like in the present work. Similar results have been reported for the conventional CVD growth of graphene [21], showing that Si and SiO_2 are inert for CVD growth processes.

3.2 Composition and bonding scheme of the B-C-N layers

A qualitative analysis of the chemical composition and bonding type of the layers has been obtained by energy filtered TEM imaging and corresponding EELS spectra. A homogeneous B, C and N distribution through the layers can be inferred in the elemental resolved TEM images reported in Figure 3 (top panel). The survey EELS

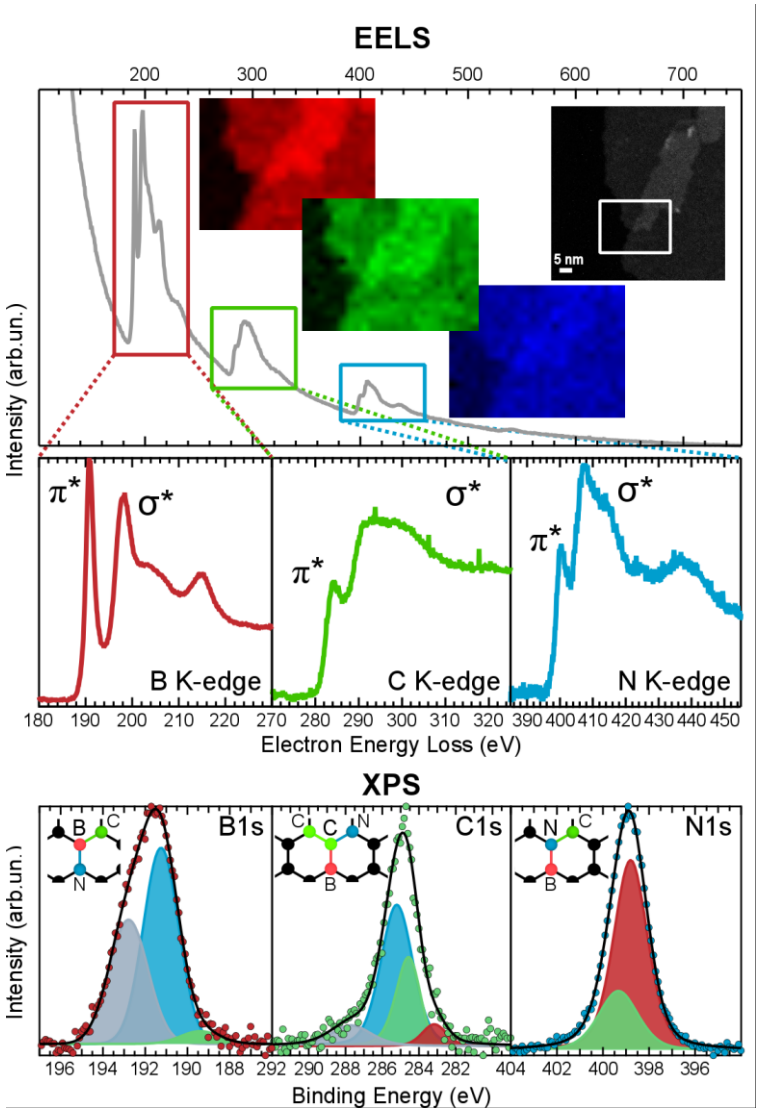

Figure 3. Top panel: EELS survey spectrum showing the K-edge absorption features characteristic of B, C and N; in the insets: zero-loss TEM image (grey) and elemental distribution of boron (red), carbon (green) and nitrogen (blue) obtained by energy filtered imaging in the zone marked by the white line. Middle panel: the zoomed regions of EELS absorption at the K-edge of B, C and N after a background subtraction. Bottom panel: XPS peaks corresponding to C 1s, N 1s and B 1s core-levels (experimental data, dots), including the overall fitting curve (black lines) and fitting components (coloured curves); the highest binding-energy fitting peak for the C and B core levels (grey curves), is associated with some oxygen contamination; in the insets, coloured sketch of the atoms and bonding-types.

spectrum taken in a wide energy loss range (Figure 3-top panel) is characterized by three intense (high intensity-to-background ratio) main energy-loss features associated to excitation from the B, C and N 1s core levels to the first unoccupied orbitals, and by a weak feature due to residual O contamination at higher energy loss. Well-resolved EELS spectra corresponding to the K-edges of B, C and N are reported, after a linear background subtraction, in Figure 3 (middle panel). All EELS features present multi-peak structures, showing the first (second) important K-edge absorption peaks at 190.8 eV (198.4 eV), 284.0 eV (290.9 eV) and 400.4 eV (407.1 eV) for B, C and N, respectively. These main and secondary absorption peaks correspond to π^* and σ^* resonances of the three elements, respectively [9, 31-34]. The observation of sharp and intense π^* resonances is a clear proof of the dominant sp^2-bonds throughout the B-C-N layers, which would be absent in case of sp^3 hybridization [31,35,36]. This result is in good agreement with Raman spectra and SAED patterns, which are also indicative of sp^2-hybridized structures in the B-C-N layers.

A further quantitative confirmation of bonding and of stoichiometry has been obtained by core-level X-ray photoelectron spectroscopy, sensitive to the topmost layers. The C 1s, N 1s and B 1s core-level XPS spectra reported in Figure 3 (bottom panel) have been taken after an ultra-high-vacuum annealing up to 480 ºC, to remove the slight ambient contamination (see Supplementary Material, Figures S12 and S13). The three core-level peaks present broad and asymmetric shapes, in good agreement with previous works in mixed B-C-N layers [4,8-10,37], where the asymmetric line-shape reveals the presence of multi-components in each core-level peak. A fitting analysis has been carried out to evaluate the position, width and relative intensity of the different contributions to each peak, using pseudo-Voigt line-shaped components (Gaussian and Lorentzian contributions, taking into account the experimental resolution and the intrinsic line shape of each core-level, respectively), after the subtraction of a Shirley-like background. The deconvolutions in different components contributing to the C, N and B 1s core-levels are also plotted in Figure 3 (bottom panel), along with the respective experimental data. Further details on the values of the fitting parameters are reported in Table 1.

Table 1. Position (binding energy, BE), peak width (full width at half maximum, FWHM), intensity normalized to the cross-section and relative intensities for the different components contributing to C, N and B 1s core level peaks.

Element	Component	BE position (ev)	Peak width (FWHM, eV)	Intensity normalised to excitation cross section σ (cps /Mbarn)	Relative intensity for each element	Relative intensity for each element (excluding oxygen)
C 1s	C-B	283.2	1.5	1940	0.08	0.09
	C-C	284.6	1.6	8020	0.33	0.37
	C-N	285.2	1.9	11710	0.47	0.54
	C-O	287.5	2.8	2920	0.12	--
N 1s	N-B	398.6	1.7	37190	0.77	0.77
	N-C	399.2	1.6	11270	0.23	0.23
B 1s	B-C	189.4	2.2	2220	0.03	0.06
	B-N	191.3	2.0	36480	0.57	0.94
	B-O	192.8	2.2	25210	0.40	--

The C-1s core level presents four components, corresponding to different bonding environments, with peak maxima at 283.2 eV (due to C-to-B bonding), 284.6 eV (C-C), 285.2 eV (C-N) and 287.5 eV (C-O), in agreement with those previously reported in mixed B-C-N layers [4,9,15,22,38-41]. The binding energy of the C-C component corresponds to the typical planar π-type bonding of graphitic sp^2 configuration, without any low-BE contributions of possible unsaturated bonds [14, 42-47]. As compared to most of the previous works on B-C-N compounds, where the dominant contribution came from C-C type bonds at 284.6 eV [4,5,9,15,38] and the side peaks represented a minor contribution to the overall spectra, here we obtained a much more mixed scheme in terms of bonding-type. In fact, the main component observed in the C 1s core level (Figure 3, bottom panel and Table 1) is due to C-N bonds, while the lower intensity C-B component is considerably increased as compared to previous works [4,5,9,15,38].

The N and B 1s signals confirm this mixed-bonding scheme. The N 1s core level shows two peaks of comparable heights and widths, at 398.6 eV (associated to the N–B component typical of h-BN and B–C–N compounds [4,9,15,37,38,48-51]) and at 399.2 eV (due to N-C bonds), with N substitutional in pyridinic and pyrrolic sites [9,40,43,52-54]. The main peak of the B 1s core level at 191.3 eV can be associated with the dominant B–N interaction [4,9,15], but also two further components must be introduced to account for the low and high-BE spectral density: a peak at 189.4 eV (due to the presence of B–C bonds [9,40,51,52]) and a more intense and broad peak at 192.8 eV (due to multicomponent B coordination to oxygen associated to unavoidable high reactivity of B with O [9,55,56]). By taking into account the peak position of the B-O component observed by XPS (Figure 3 and Table 1), these boron oxide species are likely oxygen-rich species, such as B_2O_3 [55].

The overall B:C:N ratios obtained by integrating the 1s core level peaks (taking into account the photo-excitation cross sections [57]), and excluding the oxygen components so to determine the stoichiometry of the B-C-N domains, are equal to 1.8:1.0:2.2. The B:C:N obtained with MeAB via microwave-assisted PECVD has a stoichiometry ratio closer to the 1:1:1 ratio of the precursor, than the boron-carbon-nitrides grown by conventional CVD method using the same precursor, where the average composition was much richer in C than in B and N [9].

The relative intensities for each component of B 1s, C 1s and N 1s XPS peaks have been calculated as the percentage of the total area normalized to the respective photo-excitation cross section values [57], as shown in Table 1. The significant presence of B-C, B-N, C-C and C-N bonds is observed, which imply an important mixing of all the three elements in the microwave-assisted PECVD layers. These features indicate a much more homogeneous bonding among the three elements, B, C and N, as compared to previous works, where segregation into C-rich and h-BN-rich domains was dominant [4,5,7-9,15]. Our results also point out to segregation into two phases: C-rich and h-BN-rich ones, but these appear to be highly doped by N and B, and by C, respectively. It can be seen that N-doping of C-rich phase is much higher than B-doping, which should be explained by the stronger C-N bond energy as compared to C-B bonding. In particular, more than 50% of C atoms in C-rich domains are bound to N. Previously reported results for ternary B-C-N layers reached lower doping levels of C-rich and h-BN-rich domains [7-9]. N-doping in C-rich nanodomains is even higher than the values reported

for Gr, reaching up to 3.5 at.% and 8.9 at.% in previous literature data, depending on the synthesis route [21,58].

In conclusion, both EELS and XPS confirm the establishment of the dominant mutual planar sp^2 hybridized bonds among B, C and N atoms, in agreement with Raman and SAED measurements. Furthermore, XPS results point at the actual formation of planar highly mixed B-C-N phases.

3.3 Optical and electronic transport properties

In order to investigate the effects of the observed changes in bonding configurations through the samples on the electronic band structure of the obtained B-C-N layers, optical absorption spectra have been recorded in the UV-vis region. The typical spectrum is shown in Figure 4. This spectrum presents two absorption bands in the near UV range, with peak maxima at 250 and 200 nm. This result is similar to those obtained in hybrid B-C-N layers composed by C-rich and h-BN-rich domains [4,5,9], which present a band at 270 nm corresponding to C-rich regions and another band at 200 nm from h-BN domains. However, peak positions of the optical absorption bands in Figure 4 are considerably shifted as compared to previous works (see the Supplementary Material, Figure S14). These shifts can't be ascribed to the presence of B-O species observed by XPS, since similar B-O species were already present in previously reported B-C-N layers [9]. Moreover, the optical absorption bandgap of B_2O_3 is around 6.2 eV [75], and, therefore, the corresponding absorption peak is expected to be below 200 nm. The peak position of the optical absorption band from Gr domains, both in pure Gr and Gr/h-BN patchworks, is usually observed at 268-270 nm [4,5,9,21,59], whereas it is blueshifted to 250 nm in the present B-C-N layers. Previous works on Gr samples have reported a redshift of the absorption peak induced by doping (both with electrons and holes) [60]. Therefore, the blueshift observed in the present B-C-N layers cannot be explained by electron/hole doping and suggests a change in the electronic band structure, which is ascribed to the high N- and B-doping of C-rich domains observed by XPS. In spite of these important changes, this absorption band can still be properly fitted by using a Fano model, that has been reported to describe the optical absorption band in Gr and graphitic layers due to π plasmon resonance [59,60]. This model describes this optical absorption peak as due to a direct interband transition at the M

point of the Brillouin zone (where the electronic density of states is high). The electron-hole exciton created by this transition strongly interacts with the existing continuum of electronic states. The fitting of the optical absorption band (see the blue line in Figure 5) gives the following parameters E_0=5.55eV; E_{res}=5.325eV; Γ=2.2 eV, where E_0 is the band to band transition energy at the M point singularity, E_{res} is the resonance energy of the perturbed exciton and Γ is the width relative to the resonance energy E_{res} of the perturbed exciton. As compared to the values reported for monolayer Gr (E_0=5.20 eV, E_{res}=5.02 eV, Γ=0.78 eV) [59] and B-C-N nanolayers (consisting in Gr/h-BN nanodomains) obtained by conventional CVD growth (E_0=5.20 eV, E_{res}=4.95 eV, Γ=1.56 eV) [9], the values obtained here show a considerable increase in the band to band transition energy and the resonance energy of the perturbed exciton. Such effects are a clear signature of the modification of band structure induced by doping of C-rich domains by B and N.

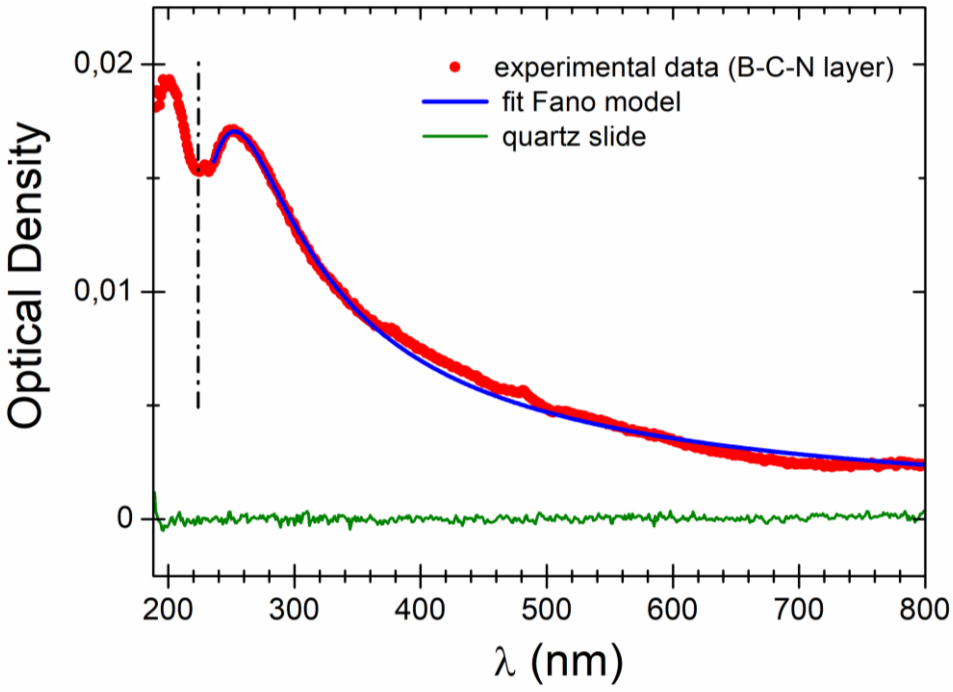

Figure 4. Optical absorption spectra of a B–C–N layer (red circles) and of the quartz substrate to confirm the recorded baseline feasibility (green line). The blue line represents the fit of the optical absorption peak by using the Fano's model. The vertical dash-dotted line indicates the position of the tail of the optical absorption band related to h-BN-rich domains.

On the other hand, the second optical absorption band peaking at 200 nm is ascribed to h-BN-rich domains [4,5,9,61]. It is difficult to obtain a precise value for the optical bandgap of this absorption peak by using Tauc or Pankove analyses, due to the overlapping of the two absorption bands present in the spectrum. However, an upper limit for this bandgap can be obtained from the position of the tail of this absorption band (marked by a vertical dashed-dotted line in Figure 4). This tail is observed at a wavelength of 223 nm, which corresponds to a photon energy of 5.56 eV. It is worth to note that this tail occurs at a longer wavelength than in h-BN domains [61] and in Gr/BN hybrid layers [9] (213 nm, as shown in the Supplementary Material). The optical bandgap related to this transition is thus redshifted (<5.56 eV in the B-C-N layer obtained here instead of 5.82-5.97 eV in h-BN [9,61]). Such a modification might be related to C-doping of h-BN nanodomains inferred from XPS data.

The two optical absorption bands present in the absorption spectrum are also consistent with the coexistence of two phases in the obtained B-C-N layers: graphitic nanodomains significantly doped with N and some B, and h-BN-rich regions doped with C. In spite of the strong tendency of the B-C-N ternary system towards segregation into C-rich and h-BN phases, we have demonstrated the efficient mutual doping of these phases by N and B, and by C atoms, respectively. The present growth method achieves the higher doping level reported so far for these systems, changing considerably the electronic band structure of the two phases. Moreover, the presence of a novel tiny absorption peak at 228 nm, between the two main absorption bands (see more details in the Supplementary Material, Figure S15), might be associated to the formation of a third mixed phase of the ternary compound, although the experimental results are not conclusive and further evidence is needed.

Further evidence of the strong modification of the electronic structure induced by doping effects are based on electronic transport measurements of the B-C-N layers. These measurements have been done by fabricating bottom-gated FETs. A typical AFM micrograph of the Au gold contacts on the B-C-N film is shown in Figure 5a. The characteristic curves of the source-drain current (I_{ds}) as a function of the applied source-drain voltage (V_{ds}) at different temperatures can be seen in Figure5b. These curves present a nonlinear behaviour (with inversion symmetry), pointing out the semiconducting nature of the obtained samples, thus forming a barrier with the electrodes, which has been also observed in other similar FETs devices [21,58,62-64].

Even at V_{ds} voltages up to 40 V, we do not observe current saturation (see the Supplementary Material, Figure S17). However, device failure is observed at V_{ds} values close to 50 V and at a current density of $0.6 \cdot 10^8$ A/m^2 (60 A/mm^2). The absence of current saturation is indicative of graphene type conduction, limited by velocity and not by the number of charge carriers. Temperature dependence of the source-drain current (I_{ds}) recorded at a source-drain voltage (V_{ds}) of 0.5 V and zero gate voltage (V_g= 0 V) is depicted in Figure 5c. The drain current does not obey an Arrhenius-type temperature dependence (see the Supplementary Material, Figure S16), but follows a Mott's two-dimensional (2D) variable range hopping (VRH) behaviour [65,66], as shown in Figure 5c. This mechanism demonstrates the 2D-type character of the B-C-N nanolayers. Moreover, it implies that the electronic transport is governed by hopping of electrons at variable ranges, a mechanism that is usually observed in amorphous and nanocrystalline materials [67]. On the other hand, the dependence of the in-plane conductivity (obtained from the slope of the I_{ds}–V_{ds} plots) on V_g has been also measured, in order to determine the n- or p-type character of the layers (Figure 5d). Previous results in pure Gr reveal an ambipolar behaviour, with a neutrality point (change from p- to n-type conductivity, corresponding to the Dirac point of Gr) close to zero gate voltage [21]. The neutrality point is shifted to positive gate voltages in B-C-N layers consisting in Gr- and h-BN domains [4,5,68]. In these samples, the conductivity is usually dominated by C-rich regions, due to the insulating nature of h-BN. The shift of the neutrality point in these samples seems to be related to small chemical doping and boundary scattering between h-BN and graphene domains [68]. A similar shift induced by confinement effects is observed in Gr nanoribbons [69]. In contrast with previously reported data in B-C-N layers, the conductivity recorded at room temperature in the present samples shows a monotonous increase with increasing the gate voltage (positive slope), indicating n-type conduction, as it can be seen in Figure 5d. This behaviour points out to a substantial change in the electronic transport properties of the B-C-N layers as compared to previous works, which should be ascribed to the high N-doping of C-rich nanodomains. Indeed, dopant N atoms can introduce strong electron donor states near the Fermi energy level [70,71], conferring the n-type character to the layers. According to data reported in N-doped Gr samples, low N-doping (<3.5 at.%) induces an ambipolar behaviour, shifting the neutrality point towards negative gate voltages [21], whereas higher N-doping levels (8.9 at.%) produce pure n-type conductivity [58]. Similar n-type doping effects have been also observed in in N-doped carbon nanotubes [72,73].

Therefore, electronic transport measurements confirm the high N-doping levels of C-rich domains observed by XPS.

Concerning the electrical conductivity of the layers at room temperature, typical values lie in the 0.1-1 S cm^{-1} range, showing slightly different values when comparing different samples or different zones in the same sample. The electron mobility at room temperature has been obtained from the dependence of I_{ds} on V_g, following the procedure used in previous works [58]. A low mobility of 2 $cm^2V^{-1}s^{-1}$ has been found. Similar values of electrical conductivity and electron mobility have been reported in other B-C-N layers [4,68], which is attributed to electron scattering at the boundaries between different conducting nanodomains.

Therefore, electronic transport measurements are consistent with the disordered character of the layers observed by Raman and TEM measurements, and with the high N-doping of C-rich nanodomains observed by XPS, which confers a n-type conductivity to the samples and induces a significant blueshift of the optical absorption band of C-rich regions.

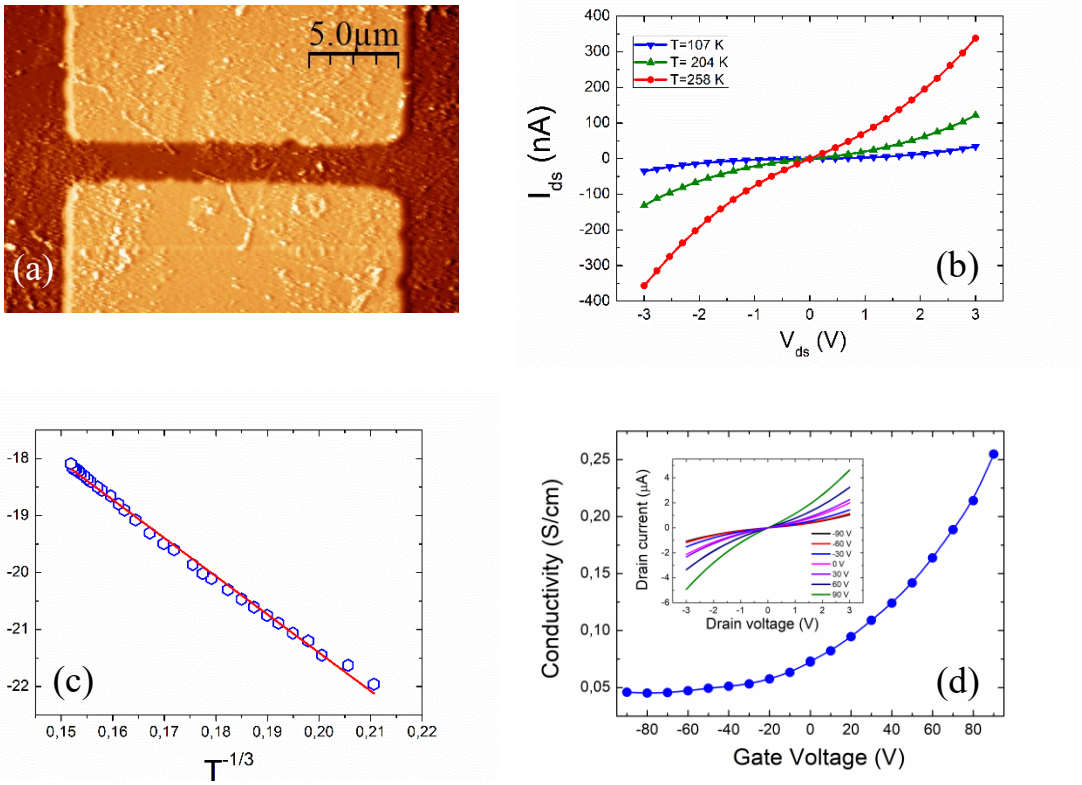

Figure 5. (a) AFM image of the FET device showing the Au electrodes (orange regions) on top of the B-C-N layer (red region). (b) Typical curves of the source to drain current as a function of the source to drain voltage at three different temperatures. (c) Plot of the temperature dependence of the source to drain current, by using a Mott 2D-VRH model. (d) Dependence of the electrical conductivity on the applied gate voltage at room temperature (293 K). The inset shows the I_{ds}-V_{ds} characteristic curves for different gate voltages. Conductivity has been obtained from the slope of I_{ds}-V_{ds} plots in the range -0.2 V < V_{ds} < 0.2 V.

4. Conclusions

This work reports a fast and direct method to grow ultrathin B-C-N layers on Cu foil substrates, based on microwave-assisted plasma-enhanced chemical vapour deposition (employing microwave radiation from a conventional home oven) by using methylamine borane as a single source molecular precursor. The method is easily scalable and presents several advantages as compared to conventional CVD methods, since it is much faster and cheaper in terms of energy and gas consumptions. Moreover, it allows changing the kinetic growth mechanism with respect to conventional CVD, what is essential to achieve homogeneous ternary B-C-N phases and to avoid segregation into C and h-BN domains. The properties of the obtained B-C-N layers have been thoroughly analysed by different techniques. Uniform and flat B-C-N layers having a thickness of about 3 nm have been obtained. More interestingly, although the layers present segregation in C-rich and h-BN-rich phases, these are highly doped by B and N, and by C atoms, respectively. Doping of C-rich domains by N is particularly pronounced. These high doping levels produce important changes in the electronic transport properties of the layers, showing n-type semiconducting behaviour. Optical absorption bands of the two phases are also substantially modified, with a reduction of the bandgap of h-BN-rich phase and a considerable blueshift of the π-band of C-rich nanodomains. The obtained results pave the way for the experimental achievement of ternary B-C-N phases in form of nanolayers, opening novel possibilities in nanoelectronics, optoelectronics and catalysis.

5. Acknowledgements

This work has been funded under FIS2014-61634-EXP and MAT2015-65203-R grants of Spanish MINECO. Technical assistance from Mr. Fernando Moreno, SIdI and Segainvex Facilities at UAM is also gratefully acknowledged. "IMDEA Nanociencia acknowledges support from the 'Severo Ochoa' Programme for Centres of Excellence in R&D (MINECO, Grant SEV-2016-0686)".

6. References

[1] da Rocha Martins J and Chacham H 2011 Disorder and segregation in B–C–N graphene-type layers and nanotubes: tuning the band gap *ACS Nano* **5** 385–93

[2] Zhu J, Bhandary S, Sanyal B, Ottosson H 2011 Interpolation of Atomically Thin Hexagonal Boron Nitride And Graphene: Electronic Structure And Thermodynamic Stability In Terms Of All-Carbon Conjugated Paths And Aromatic Hexagons *J. Phys. Chem. C* **115** 10264

[3] Guilhon I, Marques M and Teles L K 2017 Optical absorbance and band-gap engineering of (BN)1−x(C2)x two-dimensional alloys: phase separation and composition fluctuation effects *Phys. Rev. B* **95** 035407

[4] Ci L, Song L, Jin C, Jariwala D, Wu D, Li Y, Srivastava A, Wang Z F, Storr K, Balicas L, Liu F, Ajayan PM 2010 Atomic layers of hybridized boron nitride and graphene domains *Nat. Mater.* **9** 430–5

[5] Chang C-K *et al*. 2013 Band gap engineering of chemical vapour deposited graphene by in situ BN doping *ACS Nano* **7** 1333–41

[6] Levendorf M P, Kim C-J, Brown L, Huang P Y, Havener R W, Muller D A and Park J 2012 Graphene and boron nitride lateral heterostructures for atomically thin circuitry *Nature* **488** 627–32

[7] Tay R Y, Li H, Tsang S H, Zhu M, Loeblein M, Jin L, Leong F N and Teo E H T 2016 Trimethylamine borane: a new single-source precursor for monolayer h-BN single crystals and h-BCN thin films *Chem. Mater.* **28** 2180–90

[8] Nappini S, Píš I, Mentes T O, Sala A, Cattelan M, Agnoli S, Bondino F and Magnano E 2015 Formation of a quasi-freestanding single layer of graphene and hexagonal boron nitride on Pt(111) by a single molecular precursor *Adv. Funct. Mater.* **26** 1120–6

[9] Leardini F, *et al.*, 2018 Chemical vapor deposition growth of boron–carbon–nitrogen layers from methylamine borane thermolysis products, *Nanotechnology* **29** 025603

[10] Beniwal S, Hooper J, Miller D P, Costa P S, Chen G, Liu S-Y, Dowben P A, Sykes E C H, Zurek E and Enders A 2017 Graphene-like boron–carbon–nitrogen monolayers *ACS Nano* **11** 2486–93

[11] Chen G, Zakharov LN, Bowden ME, Karkamkar AJ, Whittemore SM, Garner EB, Mikulas TC, Dixon DA, Autrey T, Liu S-Y 2015 Bis-BN Cyclohexane: A Remarkably Kinetically Stable Chemical Hydrogen Storage Material *J. Am. Chem. Soc.* **137** 134−137

[12] Alton ER, Brown RD, Carter JC, Taylor RC 1959 Vapor Pressures of the Methylamine-Boranes and Ammonia-Triborane *J. Am. Chem. Soc.* **81** 3550-3551

[13] Horcas I, Fernández R, Gómez-Rodríguez JM, Colchero J, Gómez-Herrero J, Baro AM 2007 WSXM: A software for scanning probe microscopy and a tool for nanotechnology *Review of Scientific Instruments* **78** 013705

[14] Massimi L, Angelucci M, Gargiani P, Betti M G and Montoro S 2014 Metal-phthalocyanine ordered layers on Au(110): metal-dependent adsorption energy *J. Chem. Phys.* **140** 244704

[15] Massimi L, Betti M G, Caramazza S, Postorino P, Mariani C, Latini A and Leardini F 2016 In-vacuum thermolysis of ethane 1,2-diamineborane for the synthesis of ternary borocarbonitrides *Nanotechnology* **27** 435601

[16] Pearse RWB and Gaydon AG 1941 The Identification of Molecular Spectra *Chapman & Hall LTD. London*

[17] Han J, Lee J-Y, Kwon H and Yeo J-S 2014 Synthesis of wafer-scale hexagonal boron nitride monolayers free of aminoborane nanoparticles by chemical vapor deposition *Nanotechnology* **25** 145604

[18] Wen Y, Shang X, Dong J, Xu K, He J and Jiang C 2015 Ultraclean and large-area monolayer hexagonal boron nitride on Cu foil using chemical vapor deposition *Nanotechnology* **26** 275601

[19] Wang L, Wu B, Chen J, Liu H, Hu P and Liu Y 2014 Monolayer Hexagonal Boron Nitride Films with Large Domain Size and Clean Interface for Enhancing the Mobility of Graphene-Based Field-Effect Transistors *Adv. Mater.* **26** 1559–1564

[20] Pimenta M A *et al*. 2007 Studying disorder in graphite-based systems by Raman spectroscopy *Phys. Chem. Chem. Phys.* **9** 1276–91

[21] Sun Z, Yan Z, Yao J, Beitler E, Zhu Y and Tour J M 2010 Growth of graphene from solid carbon sources *Nature* **468** 549

[22] Wang H, Zhao C, Liu L, Xu Z, Wei J, Wang W, Bai X and Wang E 2016 Towards the controlled CVD growth of graphitic B–C–N atomic layer films: the key role of B–C delivery molecular precursor *Nano Res.* **9** 1221–35

[23] Cancado LG, Jorio A, Martins Ferreira EH, Stavale F, Achete CA, Capaz RB, Moutinho MVO, Lombardo A, Kulmala TS, Ferrari AC 2011 Quantifying Defects in Graphene via Raman Spectroscopy at Different Excitation Energies *Nano Lett.* **11** 3190–3196

[24] Ferrari AC 2007 Raman spectroscopy of graphene and graphite: Disorder, electron–phonon coupling, doping and nonadiabatic effects *Solid State Communications* **143** 47–57

[25] Kaniyoor A, Ramaprabhu S 2012 A Raman spectroscopic investigation of graphite oxide derived graphene *AIP Advances* **2** 032183

[26] Wang Y, Alsmeyer DC, McCreery RL 1990 Raman Spectroscopy of Carbon Materials: Structural Basis of Observed Spectra Chem. Mater. **2** 557-563

[27] Ni Z, Liu L, Wang Y, Zheng Z, Li L-J, Yu T, Shen Z, 2009 G-band Raman double resonance in twisted bilayer graphene: Evidence of band splitting and folding *Phys. Rev. B* **80** 125404

[28] Cançado LG, Takai K, Enoki T, Endo M, Kim YA, Mizusaki H, Jorio A, Coelho LN, Magalhães-Paniago R and Pimenta MA 2006 General equation for the determination of the crystallite size of nanographite by Raman spectroscopy *Appl. Phys. Lett.* **88** 163106

[29] Williams D B and Carter C B 2009 Transmission Electron Microscopy: A Textbook for Materials Science 2nd edn. (Berlin: Spinger)

[30] Qin L, Yu J, Kuang S, Xiao C and Bai X 2012 Few-atomic-layered boron carbonitride nanosheets prepared by chemical vapor deposition *Nanoscale* 4, 120

[31] Schmid H K 1995 Phase identification in carbon and BN systems by EELS *Microsc. Microanal. Microstruct* **6** 99–111

[32] Arenal R, Kociak M and Zaluzec N J 2007 High-angular resolution electron energy loss spectroscopy of hexagonal boron nitride *Appl. Phys. Lett.* **90** 204105

[33] Lu J, Gao S-P and Yuan J 2012 ELNES for boron, carbon, and nitrogen K-edges with different chemical environments in layered materials studied by density functional theory *Ultramicroscopy* **112** 61–8

[34] Wibbelt M, Kohl H and Kohler-Redlich P 1999 Multiple scattering calculations of electron-energy-loss near-edge structures of existing and predicted phases in the ternary system B–C–N *Phys. Rev. B* **59** 11739

[35] McCulloch D G, Lau D W M, Nicholls R J and Perkins J M 2012 The near edge structure of cubic boron nitride *Micron* **43** 43–8

[36] Meng Y, Mao H-K, Eng P J, Trainor T P, Newville M, Hu M Y, Kao C, Shu J, Hausermann D and Hemley R J 2004 The formation of sp3 bonding in compressed BN *Nat. Mater.* 3 111–114

[37] Sreedhara M B, Gopalakrishnan K, Bharath B, Kumar R, Kulkarni G U and Rao C N R 2016 Properties of nanosheets of 2D borocarbonitrides related to energy devices, transistors and other areas *Chem. Phys. Lett.* **657** 124–130

[38] Huang C, Chen C, Zhang M, Lin L, Ye X, Lin S, Antonietti M and Wang X 2015 Carbon-doped BN nanosheets for metal-free photoredox catalysis *Nat. Commun.* **6** 7698

[39] Sulyaeva V S, Kosinova M L, Rumyantsev Y M, Kuznetsov F A, Kesler V G and Kirienko V V 2014 Optical and electrical characteristics of plasma enhanced chemical vapor deposition boron carbonitride thin films derived from N-trimethylborazine precursor *Thin Solid Films* **558** 112–117

[40] Kang Y, Chu Z, Zhang D, Li G, Jiang Z, Cheng H and Li X 2013 Incorporate boron and nitrogen into graphene to make BCN hybrid nanosheets with enhanced microwave absorbing properties *Carbon* **61** 200–208

[41] Chiang W-H, Hsieh C-Y, Lo S-C, Chang Y-C, Kawai T and Nonoguchi Y 2016 C/BCN core/shell nanotube films with improved thermoelectric properties *Carbon* **109** 49–56

[42] Usachov D *et al.* 2011 Nitrogen-doped graphene: efficient growth, structure, and electronic properties *Nano Lett.* **11** 5401–5407

[43] Scardamaglia M, Lisi S, Lizzit S, Baraldi A, Larciprete R, Mariani C and Betti M G 2013 Graphene-induced substrate decoupling and ideal doping of a self-assembled iron phthalocyanine single layer *J. Phys. Chem. C* **117** 3019–3027

[44] Gupta B, Bernardo I D, Mondelli P, Pia A D, Betti M G, Iacopi F, Mariani C and Motta N 2016 Effect of substrate polishing on the growth of graphene on 3C–SiC(111)/Si (111) by high temperature annealing *Nanotechnology* **27** 185601

[45] Massimi L *et al.* 2015 Surface-assisted reactions toward formation of graphene nanoribbons on Au(110) surface *J. Phys. Chem. C* **119** 2427–37

[46] Di Bernardo I, Avvisati G, Mariani C, Motta N, Chen C, Avila J, Asensio MC, Lupi S, Ito Y, Chen M, Fujita T and Betti MG 2017 Two-Dimensional Hallmark of Highly Interconnected Three-Dimensional Nanoporous Graphene *ACS Omega* **2** 3691−3697

[47] Di Bernardo I, Avvisati G, Chen C, Avila J, Asensio MC, Hu K, Ito Y, Hines P, Lipton-Duffin J, Rintoul L, Motta N, Mariani C, Betti MG 2018 Topology and doping effects in three-dimensional nanoporous graphene *Carbon* **131** 258-265

[48] Sulyaeva V S, Kosinova M L, Rumyantsev Y M, Kesler V G and Kuznetsov F A 2013 PECVD synthesis and optical properties of BCXNY films obtained from N-triethylborazine as a single-source precursor *Surf. Coat. Technol.* **230** 145–51

[49] Huang F L, Cao C B, Xiang X, Lv R T and Zhu H S 2004 Synthesis of hexagonal boron carbonitride phase by solvothermal method *Diam. Relat. Mater.* **13** 1757–60

[50] Henck H, Pierucci D, Ben Aziza Z, Silly M G, Gil B, Sirotti F, Cassabois G and Ouerghi A 2017 Stacking fault and defects in single domain multilayered hexagonal boron nitride *Appl. Phys. Lett.* **110** 023101

[51] Kumar N, Moses K, Pramoda K, Shirodkar S N, Mishra A K, Waghmare U V, Sundaresan A and Rao C N R 2013 Borocarbonitrides, BxCyNz *J. Mater. Chem. A* **1** 5806–21

[52] Moses K, Shirodkar S N, Waghmare U V and Rao C N R 2014 Composition-dependent photoluminescence and electronic structure of 2-dimensional borocarbonitrides, BCxN (x=1,5) *Mater. Res. Express* **1** 025603

[53] Scardamaglia M, Struzzi C, Aparicio Rebollo F J, De Marco P, Mudimela P R, Colomer J-F, Amati M, Gregoratti L, Petaccia L and Snyders R 2015 Tuning electronic properties of carbon nanotubes by nitrogen grafting: chemistry and chemical stability *Carbon* **83** 118–27

[54] Rao CNR, Chhetri M 2018 Borocarbonitrides as Metal-Free Catalysts for the Hydrogen Evolution Reaction *Advanced Materials* 1803668 doi: 10.1002/adma.201803668

[55] Ong C W, Huang H, Zheng B, Kwok R W M, Hui V and Lau W M 2004 X-ray photoemission spectroscopy of nonmetallic materials: electronic structures of boron and BxOy *J. Appl. Phys.* **95** 3527

[56] Paul R, Voevodin A A, Zemlyanov D, Roy A K and Fisher T S 2012 Microwave-assisted surface synthesis of a boron–carbon–nitrogen foam and its desorption enthalpy *Adv. Funct. Mater.* **22** 3682–90

[57] Yeh JJ, Lindau I 1985 Atomic subshell photoionization cross sections and asymmetry parameters: $1 \leqslant Z \leqslant 103$ *Atomic Data and Nuclear Data Tables* **32** 1-155

[58] Wei D, Liu Y, Wang Y, Zhang H, Huang L and Yu G 2009 Synthesis of N-Doped Graphene by Chemical Vapor Deposition and Its Electrical Properties *Nano Lett.* **9** 1752-1758

[59] Mak KF, Shan J, Heinz TF 2011 Seeing Many-Body Effects in Single- and Few-Layer Graphene: Observation of Two-Dimensional Saddle-Point Excitons *Phys. Rev. Lett.* **106** 046401

[60] Mak KF, da Jornada FH, He K, Deslippe J, Petrone N, Hone J, Shan J, Louie SG, Heinz TF 2014 Tuning Many-Body Interactions in Graphene: The Effects of Doping on Excitons and Carrier Lifetimes *Phys. Rev. Lett.* **112** 207401

[61] Watanabe K, Taniguchi T and Kanda H 2004 Direct-bandgap properties and evidence for ultraviolet lasing of hexagonal boron nitride single crystal *Nature Mat.* **3** 404-409

[62] Fu L, Liu Y Q, Liu Z M, Han B X, Cao L C, Wei D C, Yu G, Zhu D B 2006 Carbon Nanotubes Coated with Alumina as Gate Dielectrics of Field-Effect Transistors *Adv. Mater.* **18** 181–185.

[63] Li X L, Liu Y Q, Fu L, Cao L C, Wei D C, Wang Y, Yu G 2007 Synthesis and Device Integration of Carbon Nanotube/Silica Core−Shell Nanowires *J. Phys. Chem. C* **111** 7661–7665.

[64] Kruger H, Janietz S, Sainova D, Dobreva D, Koch N, Vollmer A. 2007 Hybrid Supramolecular Naphthalene Diimide-thiophene Structures and their Application in Polymer Electronics *Adv. Funct. Mater.* **17** 3715–3723.

[65] Lopez V, Sundaram R S, Gomez-Navarro C, Olea D, Burghard M, Gomez-Herrero J, Zamora F and Kern K 2009 Chemical Vapor Deposition Repair of Graphene Oxide: A Route to Highly Conductive Graphene Monolayers *Adv. Mater.* **21** 4683–4686

[66] Cheah C Y, Gomez-Navarro C, Jaurigue L C and Kaiser A B 2013 Conductance of partially disordered graphene: crossover from temperature dependent to field-dependent variable-range hopping *J. Phys.: Condens. Matter* **25** 465303

[67] Muchharla B, Pathak A, Liu Z, Song L, Jayasekera T, Kar S, Vajtai R, Balicas L, Ajayan P M, Talapatra S and Ali N 2013 Tunable Electronics in Large-Area Atomic Layers of Boron−Nitrogen−Carbon *Nano Lett.* **13** 3476−3481

[68] Song L, Balicas L, Mowbray D J, Capaz R B, Storr K, Ci L, Jariwala D, Kurth S, Louie S G, Rubio A and Ajayan P M 2012 Anomalous insulator-metal transition in boron nitride-graphene hybrid atomic layers *Phys. Rev. B* **86** 075429

[69] Han M Y, Brant J C, Kim P 2010 Electron Transport in Disordered Graphene Nanoribbons *Phys. Rev Lett.* **104**, 056801

[70] Lim S H, Li R, Ji W, Lin J 2007 Effects of nitrogenation on single-walled carbon nanotubes within density functional theory *Phys. Rev. B* **76** 195406.

[71] Carroll D L, Redlich P, Blase´ X, Charlier J C, Curran S, Ajayan P M, Roth S, Ruhle M 1998 Effects of Nanodomain Formation on the Electronic Structure of Doped Carbon Nanotubes *Phys. Rev. Lett.* **81** 2332–2335

[72] Xiao K, Liu Y Q, Hu P A, Yu G, Sun Y M, Zhu D 2005 n-Type field-effect transistors made of an individual nitrogen-doped multiwalled carbon nanotube *J. Am. Chem. Soc.* **127** 8614–8617

[73] Terrones H, Terrones M, Hernandez E, Grobert N, Charlier J C, Ajayan P M 2000 New Metallic Allotropes of Planar and Tubular Carbon *Phys. Rev. Lett.* **84** 1716–1719

[74] Eckmann A, Felten A, Mishchenko A, Britnell L, Krupke R, Novoselov KS, Casiraghi C 2012 Probing the Nature of Defects in Graphene by Raman Spectroscopy *Nano Lett.* **12**, 3925−3930

[75] Li D, Ching WY 1996 Electronic structures and optical properties of low- and high-pressure phases of crystalline B_2O_3 *Phys. Rev. B* 54, 13616